1

Introduction

Hiroyuki Fujiwara

Gifu University, Department of Electrical, Electronic and Computer Engineering, 1-1 Yanagido, Gifu 501-1193, Japan

1.1 Hybrid Perovskite Solar Cells

Hybrid perovskites, unique materials composed of moving organic cations and rigid inorganic framework, show remarkable suitability as light absorbers of photovoltaic devices, enabling us to reach a 25% efficiency in a single-cell configuration [1] and a 29% efficiency in a tandem device configuration [1] in a rather short period of time since the first development of a hybrid perovskite solar cell in 2009 [2]. Compared with structurally complex solar cells such as Si [3, 4], GaAs [5], and $CuInGaSe_2$ [3, 6], the architecture of hybrid perovskite solar cells is surprisingly simple (Figure 1.1a); by essentially sandwiching a perovskite absorber layer between the electron transport layer (ETL) and the hole transport layer (HTL), a quite high efficiency exceeding 20% can be realized without including complicated processing steps [7–22]. For hybrid perovskites, no intentional doping is necessary and the interface recombination is suppressed quite well even though the heterogeneous interfaces are formed with ETL and HTL. Hybrid perovskite polycrystalline absorbers can be formed by a solution-based process at a surprisingly low temperature of ~100 °C [10], making the perovskite materials extremely attractive for both large-area and tandem photovoltaic applications.

Hybrid perovskites, including methylammonium lead iodide ($CH_3NH_3PbI_3$; $MAPbI_3$) and formamidinium lead iodide ($HC(NH_2)_2PbI_3$; $FAPbI_3$), are a unique form of ABX_3 perovskites consisting of organic A-site cations ($A = CH_3NH_3^+$, $HC(NH_2)_2^+$), B-site cations ($B = Pb^{2+}$, Sn^{2+}), and X-site halide anions ($X = I^-$, Br^-, Cl^-) (see Figure 1.1b). The word "hybrid" indicates that the crystal is made specifically by the combination of "organic" and "inorganic" components. In a hybrid perovskite crystal, an organic cation is confined in a cage structure formed by a BX_6 octahedron that is interconnected via all corners to form a three-dimensional perovskite network (Figure 1.1a). The semiconducting properties of hybrid perovskites arise from the inorganic BX_3 component (Section 5.4.3), and all critical phenomena of the light absorption, carrier generation, and carrier transports occur

Hybrid Perovskite Solar Cells: Characteristics and Operation,
First Edition. Edited by Hiroyuki Fujiwara.

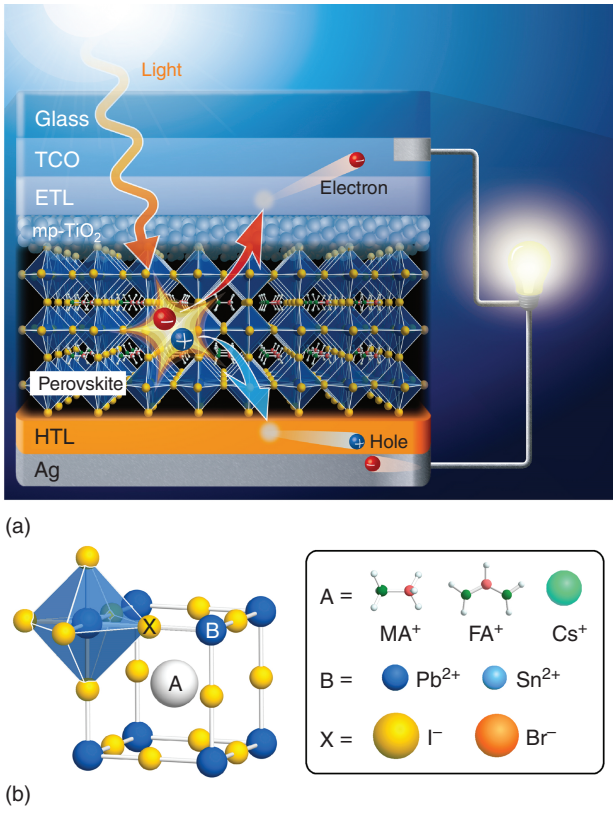

Figure 1.1 (a) Operation of a hybrid perovskite solar cell consisting of a glass/transparent conductive oxide (TCO)/electron transport layer (ETL)/mesoporous TiO_2 (mp-TiO_2)/perovskite layer ($CH_3NH_3PbI_3$)/hole transport layer (HTL)/metal electrode (Ag) structure, and (b) structure of ABX_3 perovskite crystals, whereas A is an organic (or inorganic) cation ($A = CH_3NH_3^+$ (MA^+), $HC(NH_2)_2^+$ (FA^+) or Cs^+), B is a divalent cation ($B = Pb^{2+}$ or Sn^{2+}), and X is a halide anion ($X = I^-$, Br^-, or Cl^-). In (b), the structure of a BX_6 octahedron is indicated by blue planes. The ionic radii are summarized in Table 3.3.

within the inorganic framework, while the organic cation plays an important role in determining the fundamental stability of perovskite crystals (Section 3.3).

A standard hybrid perovskite device has a structure composed of glass/transparent conductive oxide (TCO)/TiO_2 (ETL)/mesoporous TiO_2 (mp-TiO_2)/perovskite(~500 nm)/HTL/metal (Figure 1.1a). The mp-TiO_2 is the anatase phase of TiO_2 with high porosity (~60%) [23, 24], which is helpful for improving the efficiency [7, 25]. As ETL and HTL of the cells, a variety of inorganic and organic layers have been applied (see Figure 11.2). The operation of the perovskite device is straightforward; namely, the photo-electrons and holes created by light absorption are collected in the ETL and HTL, respectively, and the electrons flow through the outer circuit and recombine with holes at the HTL/metal interface.

Figure 1.2a shows the scanning electron microscope (SEM) image of a state-of-the-art hybrid perovskite solar cell with an efficiency of ~21% [19]. The absorber

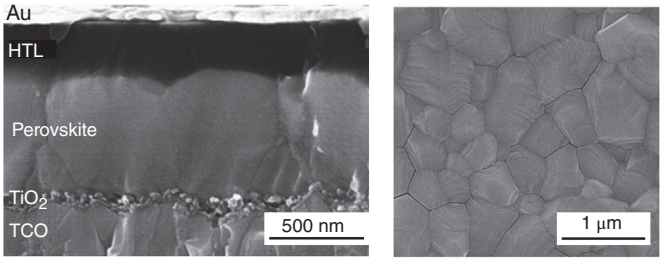

Figure 1.2 (a) Cross-sectional image of a hybrid perovskite solar cell with 20.8% efficiency and (b) surface image of the perovskite absorber layer. The hybrid perovskite layer is a triple-cation-mixed perovskite with $Cs_{0.05}FA_{0.79}MA_{0.16}Pb(I_{0.83}Br_{0.17})_3$. The solar cell in (a) has a standard device structure of TCO(SnO_2:F)/TiO_2(ETL)/mp-TiO_2/perovskite/spiro-OMeTAD(HTL)/Au. *Source*: Singh and Miyasaka [19].

of this cell is a triple-cation-mixed perovskite of $CsFAMAPb(I,Br)_3$, in which three mixed cations of $A = Cs^+$, FA^+, and MA^+ are incorporated into the $Pb(I,Br)_3$ scaffold (Chapter 3). The structure of this device is exactly the same as that of Figure 1.1a. Even though the grain size of the polycrystalline perovskite is relatively small (~1 μm in Figure 1.2b), the grain boundary does not deteriorate cell characteristics significantly (Chapter 10 and Section 11.5.3) and the high conversion efficiency can be realized.

Historically, in the first hybrid perovskite cell developed by Miyasaka's group in 2009 [2], $MAPbI_3$ nanocrystals were employed as "sensitizers," which behaved only as the photocarrier generator without the active role of carrier transport (Chapter 2). In 2012, the conversion efficiency of the sensitizer concept cells improved markedly by the adoption of a thicker $MAPbI_3$ and a more sophisticate structure of TiO_2/$MAPbI_3$/spiro-OMeTAD, reaching ~10% efficiencies [26, 27]. In 2013, Snaith's group succeeded in developing a hybrid perovskite cell, which utilizes a thick perovskite absorber (~300 nm) for both carrier generation and transport, demonstrating a remarkably higher efficiency of 15% [28].

Figure 1.3 summarizes the development of hybrid perovskite solar cells during 2013–2020 [1, 29–42]. The conversion efficiency of the world-record cell in 2020 is 25.2% with the short-circuit current density (J_{sc}) of 25.1 mA/cm^2, the open-circuit voltage (V_{oc}) of 1.18 V, and fill factor (FF) of 84.8% [1]. A high J_{sc} of ~25 mA/cm^2 has been obtained since the early research stage, and the drastic improvement of the cell efficiency originates mostly from the increase in V_{oc} and FF. One of the main advantages of hybrid perovskite solar cells is a very small J_{sc} loss (Section 11.4.2), and the current perovskite solar cell is limited by V_{oc} and FF (see Figure 12.13) [5]. The carrier collection in the perovskite devices is already 100% (Figure 11.11), and now the experimental V_{oc} (1.18 V) and FF (84.8%) become closer to the theoretical limits of V_{oc} = 1.28 V and FF = 90%, derived for $FAPbI_3$ (Table 12.1). The conversion efficiency of tandem devices is also improving in an unprecedented pace (Figure 17.10), and the mass production of perovskite/Si tandem devices is already in progress [43].

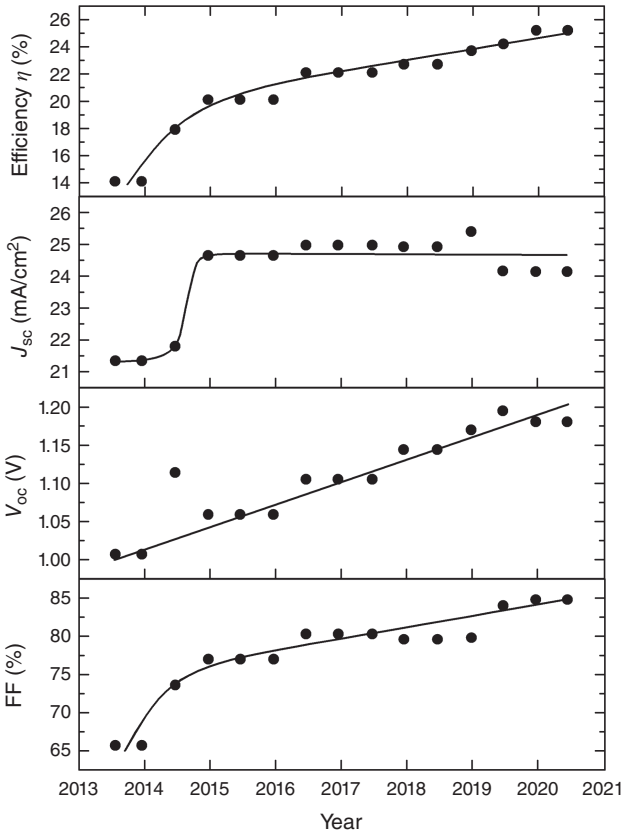

Figure 1.3 Variation of solar cell characteristics reported for record-efficiency hybrid perovskite devices during 2013–2020 [1, 29–42]. The solar cell performances described in "solar cell efficiency tables" are summarized. *Source*: Green et al. [1, 29–42].

1.2 Unique Natures of Hybrid Perovskites

Hybrid perovskites show physical properties that are surprisingly suitable for solar cells. Unlike conventional inorganic semiconductors, organic–inorganic hybrid perovskites exhibit strong dynamical motion at room temperature (Figure 1.4). In $MAPbI_3$, for example, MA^+ organic cations confined in the PbI_3 cage move (reorient) rapidly with a time scale of 5 ps (Figure 3.16). However, the movement of MA^+ is not completely random but is restricted by the hydrogen bond formed with the PbI_3^- inorganic scaffold (Figures 3.15 and 5.5). Moreover, hybrid perovskites are essentially "soft materials" and the PbI_6 octahedra show a large distortion [44, 45], as depicted in Figure 1.4. Furthermore, under the presence of the electric field, halide ions move easily through the three-dimensional inorganic network [46], causing a well-known hysteresis in current–voltage characteristics (Chapter 16). Accordingly, the dynamical structure of hybrid perovskites is quite complex, making the theoretical interpretation more challenging (Chapter 5).

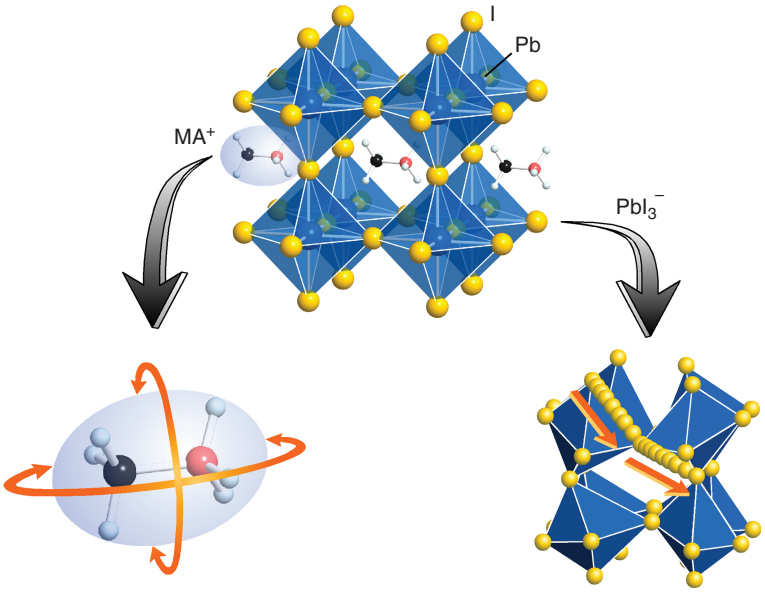

Figure 1.4 Structure of a $MAPbI_3$ perovskite crystal. The rapid reorientation of organic cations (MA^+) within the PbI_3^- inorganic cage and large distortion of the PbI_6 octahedra are illustrated. The movement of I^- under the presence of the electric field is further shown schematically by the orange arrows.

This section introduces the notable characteristics of hybrid perovskites (Section 1.2.1). In particular, the fundamental physical properties of hybrid perovskites are briefly reviewed based on the most studied $MAPbI_3$ perovskites (Section 1.2.2). We further discuss why hybrid perovskite materials are so preferable for photovoltaic devices and why high efficiency can be achieved relatively easily (Section 1.2.3).

1.2.1 Notable Characteristics of Hybrid Perovskites

Solar cells are essentially optical devices, and the strong light absorption within semiconducting absorbers is imperative. Figure 1.5 summarizes the absorption coefficient (α) spectra of representative solar cell absorbers, including $MAPbI_3$ [47], $CsFAPb(I,Br)_3$, and an Sn-based perovskite of $FAMA(Pb,Sn)I_3$. The optical data are taken from Figure 4.1 (see Appendix A for numerical values) and Ref. [48]. All the α spectra in Figure 1.5 are extracted using a reliable spectroscopic ellipsometry technique (Section 4.4). Fortunately, all hybrid perovskite materials show high α of $10^4\,cm^{-1}$ (Figure 4.1), which is comparable to other solar cell absorbers of GaAs, $CuInGaSe_2$ (CIGSe), CdTe, and Cu_2ZnSnS_4 (CZTS). Systematic theoretical and experimental analyses show clearly that hybrid perovskites are direct-transition semiconductors without any indirect nature (Section 5.4.2) and high α near the band gap (E_g) is the direct consequence of the direct optical transition (Figure 5.8). The constant α of $2\times10^4\,cm^{-1}$, observed near E_g of hybrid perovskites, leads

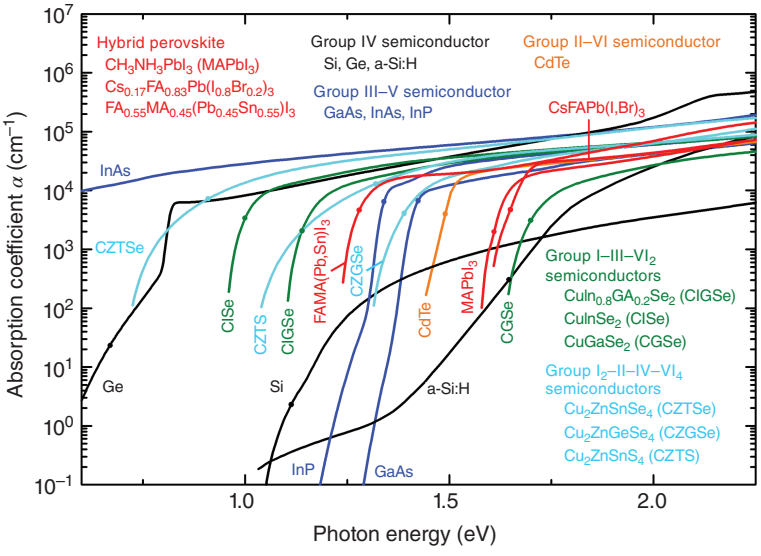

Figure 1.5 Absorption coefficient (α) spectra of representative solar cell absorbers, including $MAPbI_3$, $Cs_{0.17}FA_{0.83}Pb(I_{0.8}Br_{0.2})_3$, and $FA_{0.55}MA_{0.45}(Pb_{0.45}Sn_{0.55})I_3$. The closed circles in the figure show the band gap (E_g) energy of each absorber. All the optical results are extracted from reliable spectroscopic ellipsometry measurements. The hybrid perovskite materials show high α of 10^4 cm^{-1}, which is comparable to other solar cell absorbers of GaAs, CIGSe, and CdTe. The exact numerical values of the perovskites are summarized in Appendix A. The result of $MAPbI_3$ is taken from Ref. [47], whereas the data of $CsFAPb(I,Br)_3$ and $FAMA(Pb,Sn)I_3$ are consistent with those shown in Figure 4.1. The α spectra of all the other inorganic semiconductors are adopted from Ref. [48]. *Source*: Adopted from Fujiwara et al. [48].

to a light penetration depth of $d_p = 1/\alpha = 500$ nm, which is consistent with the experimental perovskite absorber thicknesses. In contrast, in the indirect-transition Si, α is quite low near E_g ($\sim$100 cm^{-1}), requiring a thick Si wafer of $\sim$100 μm.

The closed circles in Figure 1.5 show the E_g positions of each absorber. The E_g of $MAPbI_3$ is 1.61 eV [47, 49–51], while this value varies slightly depending on the analysis and characterization methods (Table 4.2). The E_g values of all the different halide perovskites are summarized in Table 4.3. A low-E_g perovskite material ($E_g \sim 1.2$ eV) can be formed by mixing Sn with Pb, while wider gap perovskites are generated by incorporating lighter halide atoms (Figure 4.9b). The A-site cation species also modifies E_g slightly in the case of $APbI_3$ (see Figure 4.9a). Shockley–Queisser theory (Section 12.2) indicates the favorable E_g range of solar cells to be 1.0–1.6 eV (Figure 12.1), which nicely overlaps the E_g range of hybrid perovskites.

In the operation of solar cell devices, one of the most critical parameters is the photocarrier diffusion length (L_D), which is quantitatively expressed as a product of carrier lifetime (τ) and mobility (μ) (Section 6.1). The larger μ and τ in solar cell active layers directly lead to improvement in the photovoltaic performance. Rather interestingly, μ of hybrid perovskites is not so large; in fact, μ inside the polycrystalline

grains of $MAPbI_3$ shows a moderate value of 30 $cm^2/(V\,s)$ (Figure 6.4). This μ is far smaller when compared with that of Si (1500 $cm^2/(V\,s)$, see Figure 6.7). The small μ observed in hybrid perovskites can essentially be attributed to a very large carrier–phonon interaction, as discussed in Section 6.3.4.

What makes hybrid perovskites so attractive for photovoltaic devices is a quite long τ. Figure 1.6 compares the time decays of normalized photoluminescence (PL) intensity (I_{PL}), reported for the polycrystalline thin films of $MAPbI_3$ [52], CIGSe [53], and CZTS [54]. The $MAPbI_3$ result has been obtained for a $MAPbI_3$ thin layer with a passivation layer of tri-*n*-octylphosphine oxide (TOPO). The I_{PL} of Figure 1.6 shows clearly that, in $MAPbI_3$, the photo-generated carriers have a quite long τ due to a very low carrier recombination. If single exponential decay is assumed for I_{PL}, the position of $I_{PL} = 1/e \sim 37\%$ directly provides τ (i.e. $I_{PL} = \exp(-t/\tau)$). In this case, τ values of $MAPbI_3$, CIGSe and CZTS are estimated to be 8 µs and 180 ns and 2 ns, respectively. Although the absolute τ is quite sensitive to the surface/interface and passivation conditions (Figure 6.5b) [52, 53, 55–58], τ of the hybrid perovskite is far longer than the other polycrystalline films. One remarkable advantage of hybrid perovskites is the absence of deep-level defects as revealed by density functional theory (DFT) calculations (Section 5.6) and a suppressed defect formation within the perovskite bulk layers extends τ substantially. In contrast, in CZTS solar cells, the short τ of the absorber layer makes the photocarrier collection difficult [59], resulting in a low efficiency of 11% [1]. For hybrid perovskites, notable long τ and moderate μ lead to a very large L_D of 50–175 µm in single crystals and 4–23 µm in thin films

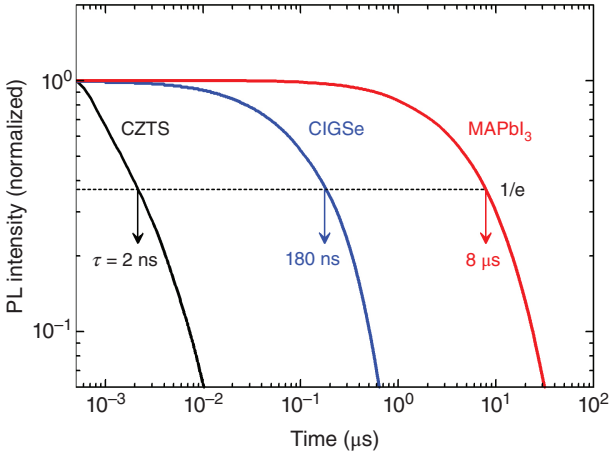

Figure 1.6 Time decays of normalized PL intensities reported for the polycrystalline thin films of $MAPbI_3$ [52], CIGSe [53], and CZTS [54]. The surface of the $MAPbI_3$ layer is passivated by a Lewis-base ligand, tri-*n*-octylphosphine oxide (TOPO). The time at which the normalized PL intensity becomes $1/e \sim 37\%$ gives the PL lifetime under the assumption of the single exponential decay (i.e. $I_{PL} = \exp(-t/\tau)$). The carrier lifetime τ obtained from this procedure is indicated for each material. Among the materials, $MAPbI_3$ shows an extraordinarily long τ of 8 µs. In the figure, the measurement noises are removed for clarity. *Source*: de Quilettes et al. [52]; Metzger et al. [53]; Phuong et al. [54].

(see Table 6.2). Recall that the perovskite absorber thickness is ~500 nm and L_D is sufficiently larger than the absorber thickness. Thus, in short, quite high efficiency of hybrid perovskite solar cells can be understood by favorable optical properties (strong light absorption and appropriate E_g) as well as the superior carrier transport characteristics represented by long τ (or L_D).

1.2.2 Fundamental Properties of $MAPbI_3$

Table 1.1 shows the room-temperature physical properties of $MAPbI_3$ determined by experimental measurements [47, 49–52, 60–95, 97–99] or theoretical calculations based on DFT [96]. This table summarizes the structural, band, optical, electric, mechanical, and thermal properties of $MAPbI_3$. The corresponding figure and table numbers in this book, from which the numerical values are extracted, are also indicated.

At room temperature, $MAPbI_3$ shows a slightly complicated tetragonal crystal structure (see Figure 3.2). The space group of the tetragonal $MAPbI_3$ has been discussed and confirmed to be *I*4*cm* [60–62], even though a slightly different assignment exists (i.e. *I*4/*mcm*) [68, 100]. However, many hybrid perovskites and their alloys exhibit a simple cubic perovskite structure (see Table 3.2). The tolerance factor (see Figure 3.9) is a critical parameter that determines the stability of perovskite crystals and the tolerance factor of $MAPbI_3$ ($t = 0.91$) falls within the ideal range of $t = 0.91$–0.98 (see Figure 3.10).

The $MAPbI_3$ exhibits superior optical properties, such as (i) direct transition, (ii) high α, (iii) sharp absorption edge (i.e. small Urbach energy of $E_U = 15$ meV), and (iv) a low exciton binding energy (Chapter 4). The direct-transition nature of the hybrid perovskite can also be confirmed from a high radiative recombination coefficient ($B = (0.1\text{–}2.3) \times 10^{-9}$ cm^3/s, see Table 8.1), which is comparable to that of a GaAs direct-transition semiconductor (0.72×10^{-9} cm^3/s). In other words, $MAPbI_3$ is a good luminescence material that can also be applied for light emitting diodes and laser diodes [101] (Chapter 8). Note that good solar cells are essentially good photo emitters (Section 11.5.1), and a high internal PL yield of 91.9% has been reported for $MAPbI_3$ [102]. The sharp band-edge absorption with $E_U = 15$ meV (see Figure 4.17a) is beneficial for lowering V_{oc} loss in the solar cells (Chapter 12) [78]. The exciton binding energy of $MAPbI_3$ (~2 meV) is smaller than the room temperature energy (i.e. $k_BT = 26$ meV) and the exciton formation is negligible in $MAPbI_3$ (Section 4.8). Interestingly, the refractive index n and high-frequency dielectric constant ε_∞ of $MAPbI_3$ are notably lower ($n = \sqrt{\varepsilon_\infty} = 2.23$) than other semiconductors (see Figure 4.3a). The low n can be interpreted by the large optical void created by the presence of the organic cations (Section 4.2). One unique optical characteristic of $MAPbI_3$ is quite strong phonon absorption, which increases the static dielectric constant to a very high value of $\varepsilon_s = 34.9$ (see Figure 4.2).

This strong phonon absorption is a key to understanding the moderate electron and hole mobility of $\mu \sim 100$ cm^2/(V s) in $MAPbI_3$ (Section 6.3.4). The intra-grain mobility in polycrystalline $MAPbI_3$ is 30 cm^2/(V s), and all the perovskite thin films show similar mobility (Figure 6.10). In the perovskite alloys, however, the

Table 1.1 Physical properties of a $MAPbI_3$ hybrid perovskite at room temperature, determined by experimental measurements and theoretical calculations based on density functional theory (DFT).

Physical property	Value	Figure and Table	References
Structural properties			
Crystal structure	Tetragonal	Table 3.2	[60]
Space group	*I4cm*		[60–62]
Lattice parameters	$a = 8.849$ Å ($\alpha = 90°$) $b = 8.849$ Å ($\beta = 90°$) $c = 12.642$ Å ($\gamma = 90°$)	Table 3.2 and Figure 3.3	[60]
Crystal volume	990.0 Å^3		[60]
Density	4.159 g/cm^3		[60]
Tolerance factor	0.91	Figure 3.10	
MA^+ reorientation time	5 ps	Figure 3.16	[63, 64]
Band properties			
Band gap	$E_g = 1.61$ eV	Figure 4.8	[47, 49–51]
E_g variation with temperature T (K)	$E_g = 1.52 + 3.04 \times 10^{-4}\ T$ eV	Figure 4.19c	
Ionization potential	−5.5 eV	Figure 11.4	[65]
Electron affinity	−3.9 eV	Figure 11.4	[65]
Effective mass	$m_e^* = 0.32\ m_0$ (electron) $m_h^* = 0.36\ m_0$ (hole)	Table 6.1	[66]
Optical properties			
Optical transition	Direct transition	Figure 5.8	[67–70]
Absorption coefficient	1.8×10^4 cm^{-1} (at 1.7 eV)	Figure 4.4	[47]
Radiative recombination coefficient	$B = (0.1–2.3) \times 10^{-9}$ cm^3/s	Table 8.1	[71–77]
Urbach energy	$E_U = 15$ meV	Figure 4.17	[78, 79]
Exciton binding energy	~2 meV	Table 4.4	[80, 81]
Refractive index	$n = 2.23$[a)]	Figure 4.2	
High-frequency dielectric constant	$\varepsilon_\infty = 5.0$	Figure 4.2	
Static dielectric constant	$\varepsilon_s = 34.9$	Figure 4.2	
Visible/UV peak	$E_1 = 2.53$ eV, $E_2 = 3.24$ eV	Figure 4.8	[47]
Longitudinal optical (LO) phonon peak	$\omega_{LO1} = 133$ cm^{-1}, $\omega_{LO2} = 40$ cm^{-1}	Figure 4.7	[82]
Transverse optical (TO) phonon peak	$\omega_{TO1} = 32$ cm^{-1}, $\omega_{TO2} = 63$ cm^{-1}	Figure 4.7	[82]

(continued)

Table 1.1 (Continued)

Physical property	Value	Figure and Table	References
Electric properties			
Electron mobility	66 $cm^2/(V\,s)$ (bulk polycrystal)	Table 6.1	[60]
	30 $cm^2/(V\,s)$ (thin film)	Figure 6.4	
Hole mobility	105 $cm^2/(V\,s)$ (single crystal)	Table 6.1	[83]
	30 $cm^2/(V\,s)$ (thin film)	Figure 6.4	
Carrier lifetime	$\tau = 10$–82 μs (single crystal)	Table 6.2	[83–86]
	$\tau = 8$ μs (thin film)	Figure 1.6	[52]
Carrier diffusion length	$L_D = 50$–175 μm (single crystal)	Table 6.2	[83–85]
	$L_D = 4$–23 μm (thin film)	Table 6.2	[75, 87, 88]
Carrier density	10^9–10^{10} cm^{-3} (single crystal)	Figure 6.3	[60, 83]
Carrier trap density	$\sim 10^{10}$ cm^{-3} (single crystal)		[83, 86, 89]
Ion density	10^{16}–10^{17} cm^{-3}	Table 16.1	[90–92]
Fröhlich parameter	$\alpha = 1.72$–2.68	Eq. (6.6)	[82, 93, 94]
Mechanical properties			
Bulk modulus	13.9 GPa	Table 6.1	[95]
Young's modulus	14.3 GPa		[95]
Hardness	0.57 GPa		[95]
Shear modulus	5.4 GPa		[95]
Poisson's ratio	0.33 (DFT)		[96]
Thermal properties			
Debye temperature	131 K (DFT)		[96]
Linear thermal expansion coefficient	43.3×10^{-6} K^{-1}		[97]
Molar heat capacity	$C_p = 189.6$ J/(K mol)		[98]
Thermal conductivity	0.5 W/(K m)		[99]

The corresponding figure and table numbers in this book, from which the numerical values are extracted, are also indicated.
a) $n = \sqrt{\varepsilon_\infty}$.

tolerance factor affects μ indirectly (Figure 6.11). As shown in Table 1.1, τ of $MAPbI_3$ single crystals is larger than that of the thin films and the resulting L_D also becomes large in single crystals (Figure 6.9). The carrier density of $MAPbI_3$ single crystals is very low ($\sim 10^{10}$ cm^{-3}) [60, 83], while the carrier concentration in the thin films can be controlled widely from p-type to n-type according to the processing condition (i.e. PbI_2/MAI precursor ratio in Figure 6.2) [103]. As mentioned

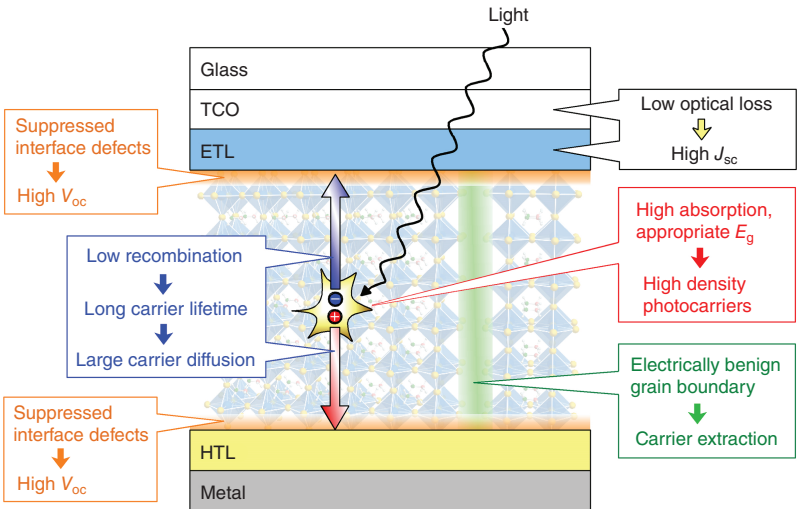

Figure 1.7 Physical features that are quite advantageous for realizing high conversion efficiencies in hybrid perovskite solar cells.

earlier, the formation of bulk defects is suppressed quite well in hybrid perovskites (Section 5.6) and the carrier trap density is very low ($\sim 10^{10}$ cm^{-3} in the single crystal) [83, 86, 89]. There are, however, many mobile ions in $MAPbI_3$ with a concentration of 10^{16}–10^{17} cm^{-3} (Table 16.1).

Hybrid perovskites are soft materials [95] and the bulk modulus of $MAPbI_3$ (13.9 GPa) is far smaller, when compared with conventional inorganic solar cell materials with corresponding values of 40–100 GPa (see Table 6.1). The thermal conductivity of $MAPbI_3$ is also very small [99]. The abovementioned characteristics show that a $MAPbI_3$ hybrid perovskite indeed has a mixed character of both inorganic and organic materials.

1.2.3 Why Hybrid Perovskite Solar Cells Show High Efficiency?

High efficiencies ($\eta > 20\%$) observed widely in hybrid perovskite solar cells can be interpreted as a consequence of several physical processes summarized in Figure 1.7. For the photocarrier generation, (i) appropriate E_g, (ii) strong light absorption (i.e. high α), and (iii) low exciton binding energy of hybrid perovskites allow the generation of high-density carriers within the absorber upon light absorption. Moreover, in standard perovskite devices, the unfavorable light absorption within TiO_2 (ETL) and TCO is suppressed quite well (see Figures 11.3 and 11.11). Sufficient carrier generation within the thin perovskite layer ($\sim$500 nm) and low parasitic absorption in the front TCO and ETL have been essential in realizing very high optical gain in the devices (Section 11.4.2).

For the carrier collection, the carrier recombination rate within the perovskite layer is very small due to a low defect (or trap) density, leading to very long τ and L_D. Unlike conventional solar cell semiconductors, in $MAPbI_3$, the electron and hole

mobilities are approximately equal (Figure 6.7) and the L_D values for electrons and holes are within the same range. This is a great advantage for solar cells as both electrons and holes need to be collected efficiently in photovoltaic devices. Remarkably, in the perovskite solar cells, the defect formation at the perovskite/ETL and perovskite/HTL interfaces is also suppressed well. The small carrier recombination within the perovskite bulk layer and at the interfaces allows us to reach high V_{oc} (Section 11.5). Note, however, that the performance of the current high-efficiency devices is mainly limited by the interface recombination (see Section 11.5.1).

Importantly, among all polycrystalline-based solar cells, hybrid perovskite devices show the highest performance, even though the grain size of the perovskites is generally small (~1 μm, see Figure 1.2). The long τ and high V_{oc} observed for the small-grain polycrystalline perovskites confirm that the grain boundary is electrically benign in hybrid perovskites. In fact, the efficient extraction of photocarriers in the grain boundary region has been confirmed experimentally (Chapter 9), although L_D is reduced slightly in the grain boundary region [104]. However, FF increases with average perovskite grain size (Figure 11.18), and thus, the larger perovskite grain is still preferable for obtaining higher efficiency.

As mentioned earlier, polycrystalline hybrid perovskite layers are formed at low temperatures (~100 °C) using a spin-coating technique. It is quite surprising that all the favorable physical characteristics shown in Figure 1.7 are obtained for such solution-processed layers.

1.3 Advantages of Hybrid Perovskite Solar Cells

Hybrid perovskite solar cells have strong advantages, in addition to high device performance exceeding 20%. In this section, as distinctive features of the perovskite cells, we focus on the large band gap tunability of hybrid perovskite absorbers (Section 1.3.1), very small V_{oc} losses in the perovskite cells (Section 1.3.2), and a very low efficiency loss at high operating temperatures (Section 1.3.3).

1.3.1 Band Gap Tunability

One important characteristic of hybrid perovskites is the large tunability of E_g. In particular, high-quality perovskite absorbers can be prepared in a wide E_g range by mixing the B-site cation (Pb–Sn) and the X-site anion (Br–I) (Chapter 4), while maintaining the sharp absorption edge (Figures 4.17 and 10.7). Figure 1.8 shows the E_g ranges of Pb- and Sn-based perovskite alloys, together with E_g of non-alloyed perovskites (see Table 4.3 for summary). The conventional E_g range of the Pb perovskites (i.e. $Cs_xFA_yMA_zPb(I,Br)_3$) is 1.55–2.3 eV, whereas the E_g can be lowered down to 1.2 eV in the Sn-based perovskites of $FA_xMA_y(Pb,Sn)I_3$ (Figure 4.10).

The large E_g tunability of hybrid perovskites enables us to develop different single and tandem cell designs. For single cells, perovskite absorbers with E_g = 1.2–1.6 eV are appropriate. Wider gap perovskites of E_g = 1.6–1.7 eV are suitable as the top cells in tandem devices employing Si bottom cells (Figure 12.17 and Chapter 17).

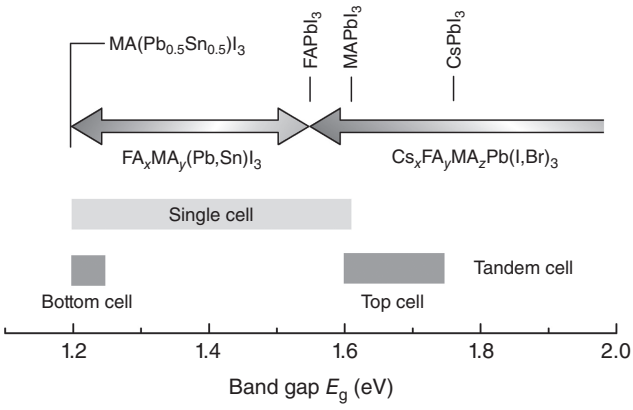

Figure 1.8 Band gap (E_g) ranges of the Pb- and Sn-based perovskite alloys of $CsFAMAPb(I,Br)_3$ and $FAMA(Pb,Sn)I_3$, together with E_g of the non-alloyed perovskites (see also Table 4.1). Note that E_g of the Sn alloys becomes the lowest around Pb/Sn = 1 due to the band gap bowing effect (see Figure 4.10c). The appropriate E_g ranges for the single and tandem cell applications are also indicated. For the perovskite/Si tandem cell, the proper E_g of the perovskite top cell is 1.6–1.7 eV (see Figure 12.18), whereas in perovskite/perovskite tandem cells, the E_g values of the top and bottom cells are 1.7–1.75 and 1.2–1.25 eV, respectively (see Figure 18.6b).

The low-E_g Sn-based perovskites ($E_g \sim 1.25$ eV) further allow the fabrication of perovskite/perovskite tandem cells (i.e. all perovskite tandem cells, Chapter 18).

Figure 1.9 summarizes the current density–voltage (J–V) characteristics reported for the state-of-the-art Sn- and Pb-based perovskite single cells as well as perovskite/Si and perovskite/perovskite tandem cells [1, 12, 21]. The solar cell parameters and absorber E_g values of these devices are also shown in Table 1.2. In the figure, a systematic variation of the J–V curve can be confirmed according to the E_g of the absorber. Remarkably, more than 20% efficiencies have been confirmed for all these cells. In particular, the efficiency of the perovskite/Si tandem device is almost 30%. The realistic efficiency of fully textured perovskite/Si devices is 36% (Table 12.2), and thus, there is a sufficient room for further improvement. Very high V_{oc} values observed already for the tandem cells (~2 V) are particularly promising for the development of higher efficiency devices. One solar cell company forecasted that the levelized cost of electricity (LCOE) of the perovskite/Si device will soon become lower than that of Si devices as early as 2022 [43].

1.3.2 High V_{oc}

One strong advantage of hybrid perovskite solar cells is quite high V_{oc}, which can be explained by the suppression of the defect formation in the bulk layer as well as at the interfaces. Figure 1.10 shows the V_{oc} of the perovskite single cell as a function of the absorber E_g [105], together with the V_{oc} limit derived from Shockley–Queisser theory (see Section 12.2 and Appendix B). For the perovskite cells with $E_g < 1.65$ eV,

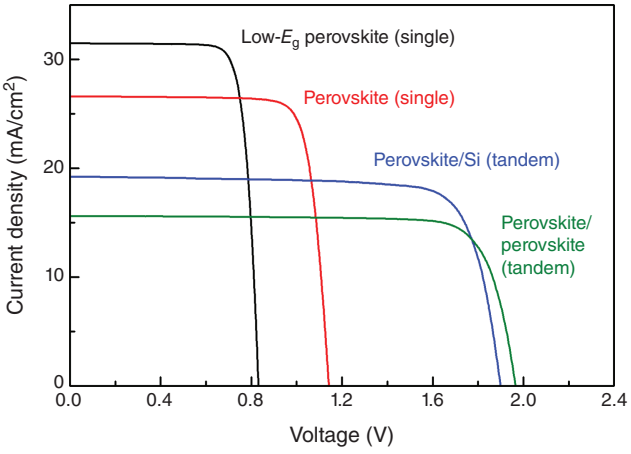

Figure 1.9 Current density–voltage (J–V) characteristics reported for the state-of-the-art Pb- and Sn-based perovskite single cells as well as perovskite/Si and perovskite/perovskite tandem devices [1, 12, 21]. The absorber of the low-E_g perovskite (single) is $FA_{0.7}MA_{0.3}(Sn_{0.5}Pb_{0.5})I_3$ [21], whereas the result of the perovskite (single) is obtained with $FAPbI_3$ with a 3.8 mol% of methylenediammonium dichloride [12]. For the perovskite/perovskite tandem cell, the top and bottom cell absorbers are $Cs_{0.05}MA_{0.05}FA_{0.9}Pb(I_{0.95}Br_{0.05})_3$ and $FA_{0.7}MA_{0.3}(Sn_{0.5}Pb_{0.5})I_3$, respectively [21]. The hybrid perovskite solar cells show the hysteresis in the J–V measurements and the J–V characteristics in the figure correspond to those obtained in the reverse scan, which show slightly higher efficiencies, compared with the forward scan. The solar cell characteristics of the corresponding cells are shown in Table 1.2. *Source:* Green et al. [1]; Min et al. [12]; Lin et al. [21].

Table 1.2 Efficiency (η) and characteristics of perovskite-based single and tandem solar cells.

Device	E_g (eV)	η (%)	J_{sc} (mA/cm^2)	V_{oc} (V)	FF	References
Sn-based perovskite single[a)]	1.22	21.1[b)]	31.4	0.83	0.808	[21]
Pb-based perovskite single[c)]	1.55[d)]	24.6	26.5	1.14	0.817	[12]
Perovskite/Si tandem	1.68[e)]/1.11	29.1	19.7	1.89	0.778	[1]
Perovskite/perovskite tandem[f)]	1.77/1.22	24.8[b)]	15.6	1.96	0.810	[21]

The band gap (E_g) values of the perovskite absorber layers are also indicated.

a) $FA_{0.7}MA_{0.3}(Sn_{0.5}Pb_{0.5})I_3$.
b) Characteristics obtained from the J–V curve sweep in the reverse direction.
c) $FAPbI_3$ with $MDACl_2$ (3.8 mol%). $MDACl_2$ is methylenediammonium dichloride.
d) E_g of $FAPbI_3$ shown in Table 4.3.
e) E_g of the perovskite shown in Table 17.1.
f) Top cell: $Cs_{0.05}MA_{0.05}FA_{0.9}Pb(I_{0.95}Br_{0.05})_3$, bottom cell: $FA_{0.7}MA_{0.3}(Sn_{0.5}Pb_{0.5})I_3$.

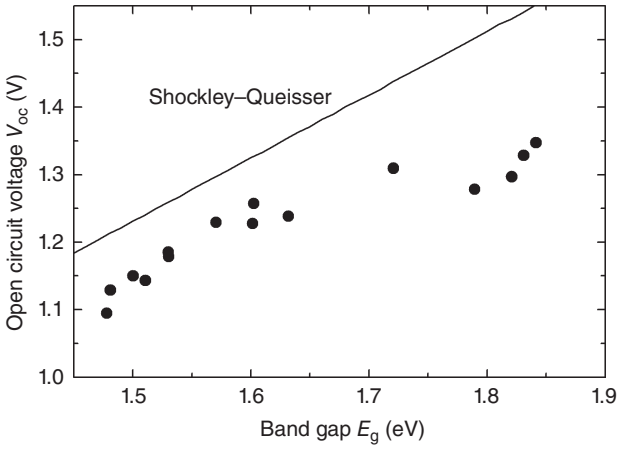

Figure 1.10 V_{oc} of hybrid perovskite single cells as a function of the absorber E_g. More complete data are shown in Figure 17.9. The closed circles show the values of the reported experimental cells, whereas the solid line indicates the V_{oc} limit derived from Shockley–Queisser theory. The numerical values of the theoretical results are shown in Appendix B. *Source*: Adapted from Jošt et al. [105].

the V_{oc} is remarkably high and V_{oc} increases with E_g without significant V_{oc} loss. In particular, a quite high V_{oc} of 1.26 V has been reported for a pure $MAPbI_3$ cell [16]. This V_{oc} is very close to the theoretical limit of 1.32 V (see Table 12.1), with the V_{oc} loss of only 60 mV. In realizing such a high V_{oc} in the perovskite cells, the suppression of the pinhole and the interface defects is critical (see Figure 11.14). Note that the formation of interface defects is particularly sensitive to the selection of ETL and HTL. In other words, the maximum V_{oc} is determined by the total amount of defects formed at the perovskite/ETL and perovskite/HTL interfaces (Figures 11.15 and 11.16), provided that L_D of the bulk layer is sufficiently long. The introduction of sophisticated passivation layers in the perovskite rear interfaces is quite effective in reducing the interface recombination and thus obtaining high V_{oc} (see Figure 11.17).

When the E_g of the perovskite becomes larger (>1.65 eV), however, the V_{oc} tends to become lower than the theoretical value (see also Figures 17.9 and 18.10a). This phenomenon can be interpreted by the strong instability observed in $APb(I,Br)_3$ perovskites with high Br contents; namely, upon light illumination, mixed I–Br perovskites show a phase segregation into the I-rich and Br-rich regions [106, 107], which in turn lowers the effective E_g (see Figure 8.7), leading to a lower V_{oc}. Numerous attempts have been made to suppress the phase separation effects (Section 18.3.3) but a new breakthrough is still necessary to suppress the light-induced segregation observed in wide-gap Br-based perovskites. Recall from Figure 1.8, however, that high-quality perovskites with $E_g < 1.65$ eV fulfill the E_g requirement necessary for top cells in perovskite/Si tandem devices (Figure 12.17), whereas the wide-gap perovskites become particularly important for all perovskite tandem devices (Figures 14.16b and 18.6b).

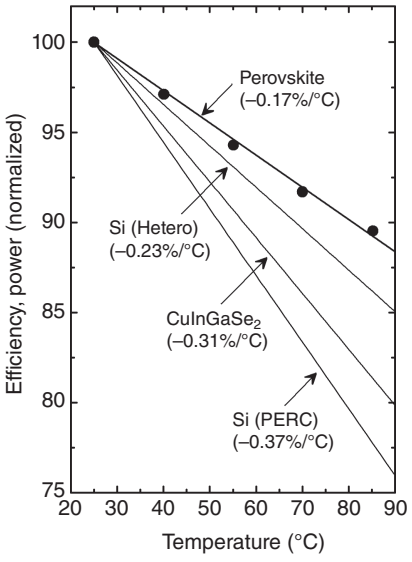

Figure 1.11 Variation of normalized conversion efficiency (or output power) with solar cell (or module) operating temperature for hybrid perovskite [108], conventional Si (i.e. PERC: passivated emitter and rear cell) [109–111], Si heterojunction [112], and $CuInGaSe_2$ [113, 114] solar cells. The temperature coefficients (i.e. the slope of efficiency variation for temperature) obtained for each cell (or module) are indicated in parentheses. The absorber material for the hybrid perovskite cell is $Cs_{0.05}FA_{0.79}MA_{0.16}Pb(I_{0.83}Br_{0.17})_3$, and the closed circles show the measured points for a 18.3% efficient p-i-n device [108].

1.3.3 Low Temperature Coefficient

Photovoltaic devices rarely operate at room temperature and high power output is necessary even under high-temperature operation conditions. Figure 1.11 shows the variation of normalized conversion efficiency (or output power) with solar cell (or module) operating temperature for hybrid perovskite [108], conventional Si (i.e. PERC: passivated emitter and rear cell) [109–111], Si heterojunction [112], and $CuInGaSe_2$ [113, 114] solar cells. Among these photovoltaic devices, the perovskite shows the lowest temperature coefficient (TC) of −0.17%/°C, which is far better than the conventional Si module that shows TC of −0.37%/°C. It is quite remarkable that nearly 90% efficiency is maintained in the perovskite device even at a high operating temperature of 85 °C.

The solar cell efficiency reduction at higher temperature essentially originates from the reduction of V_{oc}. In general, this V_{oc} reduction can be explained by two factors; (i) the decrease of E_g at high temperature and (ii) the increase of blackbody radiation with temperature that in turn increases the J_0 dark current (see Figures 12.5a and 12.6b). Remarkably, unlike conventional tetrahedral-bonding semiconductors (i.e. Si, GaAs, CdTe, and $CuInGaSe_2$), E_g of hybrid perovskites increases with temperature (Figure 4.19), which is quite beneficial to improve TC. The interface properties also affect TC, and indeed, high-efficiency Si heterojunction solar cells exhibit better TC, if compared with the conventional Si PERC cells [112]. Thus, the combination of a hybrid perovskite top cell with a Si heterojunction bottom cell is quite favorable in the view point of the TC.

1.4 Challenges for Hybrid Perovskites

For hybrid perovskite solar cells, critical challenges remain, even though quite high device efficiencies have already been realized. One significant drawback

of hybrid perovskites that limit practical applications as photovoltaic materials is strong instability (Chapter 15). Specifically, hybrid perovskites are inherently unstable and exhibit strong phase changes upon light illumination, temperature increase, and exposure to humid air [115–121]. Thus, a major challenge exists for improved stability of the perovskite solar cells. In addition, in a large-area perovskite photovoltaics, the demonstration of high conversion efficiency becomes increasingly difficult, if compared with small-area devices. Furthermore, hybrid perovskites contain a toxic Pb element, which is environmentally detrimental.

In this section, I briefly review weak points of hybrid perovskite solar cells. Section 1.4.1 explains the instability of hybrid perovskite crystals, which is the most serious problem for device applications. In Section 1.4.2, we further see the latest development for the large-area devices. In the final section (Section 1.4.3), we discuss the toxicity of Pb- and Sn-based compounds formed by the decomposition of hybrid perovskites.

1.4.1 Requirement of Improved Stability

Under light illumination, humid-air (H_2O/O_2) exposure and high temperatures, hybrid perovskites transform into PbI_2-dominated phases [115–121]. Figure 1.12 indicates the changes of a thin $MAPbI_3$ polycrystalline layer (50 nm) observed after the temperature increase (i.e. (a)→(c)) [47] and exposure to humid air (i.e. (a)→(f)) [121]. Figure 1.12a shows the surface image of a $MAPbI_3$ layer formed by co-evaporation at room temperature, and this layer consists of very small $MAPbI_3$ grains. Rather remarkably, larger $MAPbI_3$ grains are formed by thermal annealing at a temperature as low as 80 °C (see Figure 1.12b). This temperature is far lower than the thermal annealing (or process) temperatures of other semiconductors including Si, CdTe, and CIGSe. As we have seen in Figure 1.11, a temperature of 80 °C is well within the operating temperature of solar cells, but this temperature corresponds to the annealing temperature for the hybrid perovskite.

When $MAPbI_3$ is maintained at an elevated temperature of 100 °C for 45 minutes, a thermal desorption of volatile MA components occurs, leading to the formation of PbI_2 polycrystals (Figure 1.12c). Note that, in conventional solution-based approaches, the process temperatures of hybrid perovskites are ∼100 °C [10] and the strong phase variation observed at ∼100 °C is not surprising. Accordingly, easy formation of the hybrid perovskite phase at low temperatures has a natural drawback of thermal instability. Importantly, the thermal stability can be improved if a heavier organic cation (i.e. FA^+) is adopted [122], and indeed, $FAPbI_3$ is stable up to 150 °C (see also Figure 3.14). The $CsFAPb(I,Br)_3$ perovskites, which show better thermal stability than $MAPbI_3$, are frequently employed for solar cell fabrications [123–126], although a triple-cation-mixed perovskite, $CsFAMAPb(I,Br)_3$, is now quite popular as an absorber material [18–21] (Chapter 13).

When hybrid perovskite crystals are exposed to humid air, the perovskite phase is transformed completely to hexagonal-shaped PbI_2/hydrate crystals even at a low relative humidity of 40% (see Figure 1.12d,e). Hybrid perovskites are ionic crystals, and the presence of H_2O leads to the decomposition of the perovskite structures

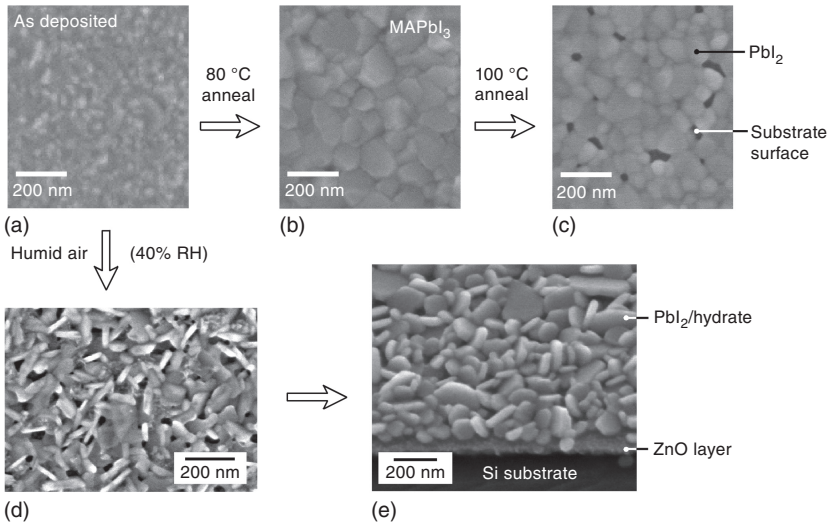

Figure 1.12 Structural changes of a thin $MAPbI_3$ polycrystalline layer (50 nm) observed after the temperature increase (i.e. (a) → (c)) and exposure to humid air (i.e. (a) → (e)). The SEM image of (a) shows the surface morphology of a $MAPbI_3$ layer formed on a ZnO/Si substrate by co-evaporation at room temperature. The surface images of (b) and (c) were obtained after thermal annealing at 80 and 100 °C for 45 minutes, respectively. The thermal annealing at 80 °C leads to the large grain formation, whereas the 100 °C annealing induces the phase transformation to PbI_2. In (d), the phase change of $MAPbI_3$ observed after the exposure to humid air (40% relative humidity, 48 hours) is shown. The image of (e) was obtained by further annealing the structure of (d) at 100 °C, but this thermal annealing does not change the structure and morphology. The exposure to humid air leads to the formation of PbI_2/hydrate crystals. *Source*: (a–c) Shirayama et al. [47]; (d, e) Shirayama et al. [121].

(Section 15.3). For the suppression of the degradation by humid air, the introduction of protective (passivation) layers at the solar cell rear interfaces has been quite effective [127–131].

Hybrid perovskites also show instability for light illumination (Figure 15.9) [115–119], and the strong light-induced phase segregation further occurs for mixed-halide perovskites [106, 107], as mentioned earlier. In the presence of an electric field, the halide ions migrate (see Figure 1.4), modifying the J–V characteristics (Chapter 16). The Sn-based perovskites are more unstable, compared with the Pb-based perovskites, due to the rapid oxidation of Sn^{2+} to Sn^{4+} in air [132]. The large instability observed in hybrid perovskites owes to the nature of chemical bonding; namely, for the inorganic framework of PbI_3^-, for example, the overlap of the wave functions between Pb and I atoms is weak, and the electronic charges of Pb and I are isolated (Figure 5.6) due to the antibonding character of the Pb—I bonds (see Figure 5.12). Thus, hybrid perovskites lack the strong bonding character and the Pb—I bonds are easily broken by external factors such as electronic excitation, electric field, temperature, and humidity.

For evaluating the stability of hybrid perovskite solar cells, a single degradation process of either heat, humidity, or light illumination may not be sufficient as the

solar cells are operated in more extreme conditions of simultaneous strong light illumination, high temperatures, and high humidity. Accordingly, extensive efforts continue to find the long-term stability of hybrid perovskite solar cells.

1.4.2 Large-Area Solar Cells

Different types of large-area photovoltaic modules (i.e. single and tandem devices) can be formed for hybrid perovskites because of the high E_g tunability. For the perovskite single modules, however, the realization of high module efficiencies becomes more challenging, if compared with wafer-based perovskite/Si tandem devices, as described below.

Figure 1.13 shows the conversion efficiencies of record-efficiency devices (hybrid perovskite, Si, and CIGSe) as a function of the cell (or module) area. The data are taken from Ref. [1]. For hybrid perovskites, a quite high efficiency of $\eta = 25.2\%$ has been obtained for small-area devices (0.09 cm^2). Recently, a very high efficiency of 17.9% has been realized for the large-area module with a size of 30×30 cm^2 (aperture area: 802 cm^2, see inset) [133], which was formed by an inkjet printing technology [134]. Over the years, the efficiency of the large-area devices has improved rapidly [35–42], but the efficiency is still lower than the small-area devices. The same trend can also be confirmed for CIGSe modules.

For thin-film large-area modules, it is more difficult to obtain high efficiency due to the essential requirements of (i) very high uniformity for all the constituent layers without the formation of pinhole, (ii) thicker TCO layers, compared with small-area devices, and (iii) increase of dead area (3–10%) due to the formation of

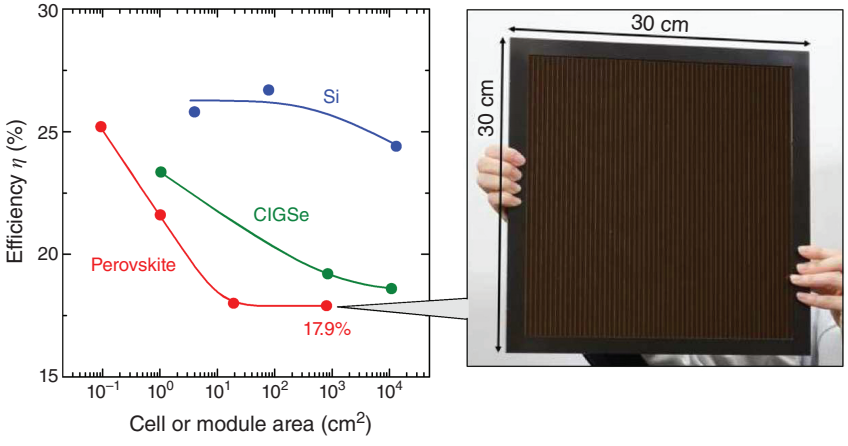

Figure 1.13 Conversion efficiencies of record efficiency devices (hybrid perovskite, Si, and CIGSe) as a function of the cell (or module) area. The data are taken from Ref. [1]. The inset shows the image of a large-area hybrid perovskite module with a size of 30×30 cm^2 (aperture area: 802 cm^2), which was fabricated by Panasonic using an inkjet printing technology [133]. A very high efficiency of 17.9% has been reported for the large-area module. *Source*: Photograph of the large-area module is taken from Ref. [133] with permission.

series interconnections [134]. The large-area modules consist of a large number of rectangular-shaped subcells (see Figure 1.13), and the current is flowing by recombination at each subcell. In other words, J_{sc} of the module is determined by the lowest J_{sc} among all the subcells and high-quality control is necessary for all the layers. Moreover, in the large-area module, the carriers need to transport over longer distances, compared with small-area devices, and thicker TCO layers are generally necessary to lower series resistance. Nevertheless, if a thick TCO layer is employed, the J_{sc} loss increases due to the strong light absorption by free carriers in TCO [59]. The free carrier absorption in TCO increases in low energies and its effect becomes significant in the devices with lower E_g [135]. In this point of view, the Pb-based perovskite single module is more advantageous than the Sn-based perovskite single module.

In contrast to the perovskite and CIGSe modules, the efficiency of Si devices remains high in Figure 1.13 even when the module area is increased. This is the result of a simple quality control that can be adopted in wafer-based Si devices with a size of $15 \times 15\,cm^2$. Specifically, the conversion efficiencies of each Si device can be checked in advance before forming the large module. Thus, high-efficiency modules can be formed by simply selecting high performance cells, while some cells with poor performance are utilized as a lower output module. Consequently, a better quality control can be realized for wafer-based perovskite/Si tandem modules, compared with large-area monolithic single modules. Note, however, that the structure of the tandem cells (see Figure 12.14a, for example) is far more complicated than that of the single cells, and there are technological challenges for the tandem devices.

In the large-area perovskite/perovskite or perovskite/CIGSe modules, the tandem-type subcells are formed, and two current matching conditions for the top and bottom cells as well as each subcell need to be established. The thick TCO layer is also required for this type of module and the high-mobility TCO becomes important to gain sufficient J_{sc} particularly for low-E_g bottom cells [135, 136]. Accordingly, technological hurdles for obtaining better efficiencies are expected to be higher for these modules.

1.4.3 Toxicity of Pb and Sn Compounds

High toxicity of a Pb heavy metal is a serious problem that cannot be avoided in Pb-based hybrid perovskite devices. Although the Pb metal content in a hybrid perovskite solar panel ($\sim 1\,m^2$) is only a few hundred milligrams, its environmental impact could be very large [137–139]. For CdTe solar modules, the hazardous effect of a Cd heavy metal is also taken seriously. However, CdTe is a thermally and chemically stable compound, while hybrid perovskites are unstable and show a very high solubility for water [137, 138]. For the perovskite modules, worst case scenarios are that (i) the breakage of the solar panels under strong storm and flooding leads to the accumulation of hazardous compounds as a result of the transportation by soil water and (ii) firing of the modules causes the emission of toxic fumes, creating a very damaging environment for living species.

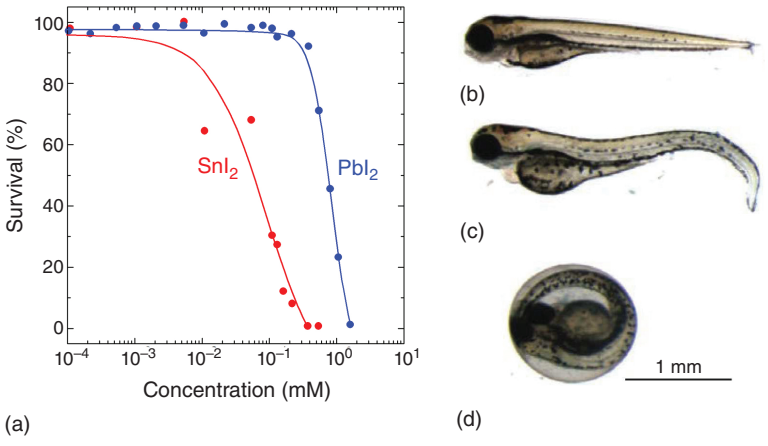

Figure 1.14 (a) Survival rate (day 4) of zebrafishes exposed to aqueous solutions with different concentrations of SnI_2 and PbI_2 toxicant and the photographs of (b) healthy zebrafish, (c) zebrafish exposed to PbI_2 (1×10^{-2} mM), and (d) zebrafish exposed to SnI_2 (1.6×10^{-1} mM). The SnI_2 is more hazardous than PbI_2. *Source*: Babayigit et al. [137].

The toxicity of Pb and Sn is well studied and, when Pb is introduced into a human body, it accumulates in bone with a very long half-life of 20–30 years [138], causing serious health problems. Although Sn-based perovskites are often treated as a more environmentally friendly alternative to Pb-based perovskites, SnI_2 formed by the decomposition of Sn-based perovskites is more lethal than PbI_2 [137, 138]. Figure 1.14 shows the survival rate (day 4) of zebrafishes exposed to aqueous solutions with different concentrations of SnI_2 and PbI_2 toxicant [137]. It can be seen that the survival rate is much lower in the SnI_2 solution than in PbI_2, and both SnI_2 and PbI_2 have serious impacts on the fish growth. The detrimental effect of SnI_2 can be interpreted by the reaction pathways of SnI_2 in water [137]:

$$8SnI_2 + 4H_2O + O_2 \rightarrow 2SnI_4 + 6Sn(OH)I + 2HI \tag{1.1}$$

where SnI_4 further decomposes into

$$SnI_4 + 2H_2O \rightarrow SnO_2 + 4HI \tag{1.2}$$

The harmful influence of SnI_2 largely originates from the formation of hydroiodic acid (HI), which reduces the pH of the solution to a very low level (pH ~ 2 at a 1 mM concentration). In contrast, the reaction of PbI_2 in H_2O is proposed as follows [137]:

$$PbI_2 + H_2O \rightarrow Pb(OH)I + HI \tag{1.3}$$

Thus, the HI formation is more suppressed for PbI_2, with a milder pH of 5 at a 1 mM level. Consequently, environmental health effects are not simply determined by the character of elements but by the nature of chemical compounds.

By considering the above, roof-top application of hybrid perovskite modules is difficult and large-area operations as solar farms are more appropriate. The structural failure of photovoltaic modules could give a significant influence on environment

and health; therefore, fail-safe measures for the encapsulation of photovoltaic modules are important. Similar to CdTe solar panels, cost-effective and environmentally friendly 100% recycling programs are also required for hybrid perovskite modules.

1.5 Overview of this Book

This book aims to provide overall understanding for unique hybrid perovskite photovoltaics, covering both the fundamental characteristics of hybrid perovskites (Part I) and the outstanding features of hybrid perovskite photovoltaics (Part II). In this book, after the general introduction (this chapter), the overview of hybrid perovskite solar cells (Chapter 2) is presented. In particular, Chapter 2 describes the short summary for the development and advance of hybrid perovskite solar cells, featuring the key aspects of the perovskite devices.

In Part I of this book (Chapters 3–10), the fundamental properties of hybrid perovskites, which are necessary to interpret the remarkable performance of the perovskite devices, are described. Specifically, in Chapter 3, the crystal structures of various hybrid perovskites and their secondary phase materials are explained. The understanding of the detailed perovskite structures described in Chapter 3 is critical in interpreting the physical properties and stability of hybrid perovskite crystals. Chapter 4 provides descriptions of the optical properties of hybrid perovskites, explaining the strong advantages of hybrid perovskites as light absorbers. Chapter 5 focuses on band and defect properties of hybrid perovskites, determined by DFT. In particular, this chapter emphasizes that hybrid perovskites are direct transition semiconductors and the deep-defect formation is negligible. In Chapter 6, the superior carrier transport properties of hybrid perovskites are described. This chapter provides detailed interpretations for very long carrier diffusion length in hybrid perovskites.

Hybrid perovskite materials show complex ferroelectricity, and their unique ferroelectric characters are described in Chapter 7. The favorable PL properties of hybrid perovskites (Chapter 8) are important characteristics, and the understanding of the PL result is critical for the interpretation of the efficiency loss mechanism in the perovskite solar cells. Chapter 9 describes the physical properties of the perovskite grain boundary. This chapter further reviews the latest developments of the grain-boundary engineering. In Chapter 10, the roles of organic center cations in hybrid perovskite crystals are introduced in the optical point of view.

In Part II of this book (Chapters 11–18), working principles for different types of hybrid perovskite photovoltaics are explained. In this part, the operational principles and important features of hybrid perovskite solar cells are described. Specifically, Chapter 11 shows that hybrid perovskite solar cells have very simple structures and their operation is quite straightforward. The latest approaches for the interface passivation are also introduced in this chapter. In Chapter 12, efficiency limits of single and tandem devices are deduced theoretically, and all the fundamental aspects necessary to understand the theoretical physical limits of the solar cells are explained. With respect to emerging hybrid perovskite devices, mixed-cation

perovskites (Chapter 13) and Sn-based perovskites (Chapter 14) are particularly important. In Chapter 13, the authors review the critical variations of hybrid perovskite cell characteristics by A-site cation mixing. The rapid advancement of low-gap Sn-based perovskites and the key factors for the efficiency improvements are explained in detail in Chapter 14.

As mentioned earlier, the stability of hybrid perovskite devices is the most serious problem and this vital issue is treated in Chapter 15. Furthermore, hysteresis that appears in the *J*–*V* curves of hybrid perovskite cells is a complex phenomenon. The physical origin of this problematic hysteresis character is presented in Chapter 16.

In the final two chapters (Chapters 17 and 18), the basic and latest developments of hybrid perovskite tandem devices are reviewed. In Chapter 17, the tandem devices formed by the combination of hybrid perovskite solar cells with Si and CIGSe devices are introduced. The perovskite/Si tandem technology is developing fast with an unprecedented pace and could become a field of main interests in near future. All perovskite tandem cells with a Pb-based perovskite top cell and an Sn-based perovskite bottom cell also show rapid advancement. In Chapter 18, the fundamental and advanced concepts of all perovskite tandem cells are reviewed. The abovementioned overall descriptions allow us to gain in-depth knowledge for the basic characteristics of hybrid perovskites and to further understand the fundamental and advanced aspects of hybrid perovskite solar cells.

Acknowledgment

The author acknowledges Tatsuya Narikuri of Gifu University for assisting the preparation of this chapter. The author would like to thank the following students of Gifu University for helping the preparation of figures that appear in this chapter: Yoshitsune Kato (Figures 1.1 and 1.7), Yukinori Nishigaki (Figures 1.3, 1.5, and 1.13), Kazuya Shibata (Figures 1.4 and 1.6), Tomoya Kobayashi (Figure 1.9), Ryo Ishihara (Figures 1.10 and 1.14), and Kohei Oiwake (Figure 1.11).

References

1 Green, M.A., Dunlop, E.D., Hohl-Ebinger, J. et al. (2020). *Prog. Photovoltaics Res. Appl.* 28: 629.
2 Kojima, A., Teshima, K., Shirai, Y., and Miyasaka, T. (2009). *J. Am. Chem. Soc.* 131: 6050.
3 Luque, A. and Hegedus, S. (2011). *Handbook of Photovoltaic Science and Engineering*. West Sussex, UK: Wiley.
4 Nakane, A., Fujimoto, S., and Fujiwara, H. (2017). *J. Appl. Phys.* 122: 203101.
5 Kato, Y., Fujimoto, S., Kozawa, M., and Fujiwara, H. (2019). *Phys. Rev. Appl.* 12: 024039.
6 Hara, T., Maekawa, T., Minoura, S. et al. (2014). *Phys. Rev. Appl.* 2: 034012.
7 Correa-Baena, J.-P., Saliba, M., Buonassisi, T. et al. (2017). *Science* 358: 739.

8 Jena, A.K., Kulkarni, A., and Miyasaka, T. (2019). *Chem. Rev.* 119: 3036.
9 Yang, W.S., Park, B.-W., Jung, E.H. et al. (2017). *Science* 356: 1376.
10 Saliba, M., Correa-Baena, J.-P., Wolff, C.M. et al. (2018). *Chem. Mater.* 30: 4193.
11 Shin, S.S., Yeom, E.J., Yang, W.S. et al. (2017). *Science* 356: 167.
12 Min, H., Kim, M., Lee, S.-U. et al. (2019). *Science* 366: 749.
13 Jeon, N.J., Na, H., Jung, E.H. et al. (2018). *Nat. Energy* 3: 682.
14 Chiang, C.-H. and Wu, C.-G. (2018). *ACS Nano* 12: 10355.
15 Saliba, M., Matsui, T., Domanski, K. et al. (2016). *Science* 354: 206.
16 Liu, Z., Krückemeier, L., Krogmeier, B. et al. (2019). *ACS Energy Lett.* 4: 110.
17 Jiang, Q., Chu, Z., Wang, P. et al. (2017). *Adv. Mater.* 29: 1703852.
18 Saliba, M., Matsui, T., Seo, J.-Y. et al. (2016). *Energy Environ. Sci.* 9: 1989.
19 Singh, T. and Miyasaka, T. (2017). *Adv. Energy Mater.* 8: 1700677.
20 Matsui, T., Yamamoto, T., Nishihara, T. et al. (2019). *Adv. Mater.* 31: 1806823.
21 Lin, R., Xiao, K., Qin, Z. et al. (2019). *Nat. Energy* 4: 864.
22 Tong, J., Song, Z., Kim, D.H. et al. (2019). *Science* 364: 475.
23 Docampo, P., Guldin, S., Stefik, M. et al. (2010). *Adv. Funct. Mater.* 20: 1787.
24 Lin, J., Heo, Y.-U., Nattestad, A. et al. (2015). *Sci. Rep.* 4: 5769.
25 Cai, M., Ishida, N., Li, X. et al. (2018). *Joule* 2: 296.
26 Lee, M.M., Teuscher, J., Miyasaka, T. et al. (2012). *Science* 338: 643.
27 Kim, H.-S., Lee, C.-R., Im, J.-H. et al. (2012). *Sci. Rep.* 2: 591.
28 Liu, M., Johnston, M.B., and Snaith, H.J. (2013). *Nature* 501: 395.
29 Green, M.A., Emery, K., Hishikawa, Y. et al. (2013). *Prog. Photovoltaics Res. Appl.* 21: 827.
30 Green, M.A., Emery, K., Hishikawa, Y. et al. (2014). *Prog. Photovoltaics Res. Appl.* 22: 1.
31 Green, M.A., Emery, K., Hishikawa, Y. et al. (2014). *Prog. Photovoltaics Res. Appl.* 22: 701.
32 Green, M.A., Emery, K., Hishikawa, Y. et al. (2015). *Prog. Photovoltaics Res. Appl.* 23: 1.
33 Green, M.A., Emery, K., Hishikawa, Y. et al. (2015). *Prog. Photovoltaics Res. Appl.* 23: 805.
34 Green, M.A., Emery, K., Hishikawa, Y. et al. (2016). *Prog. Photovoltaics Res. Appl.* 24: 3.
35 Green, M.A., Emery, K., Hishikawa, Y. et al. (2016). *Prog. Photovoltaics Res. Appl.* 24: 905.
36 Green, M.A., Emery, K., Hishikawa, Y. et al. (2017). *Prog. Photovoltaics Res. Appl.* 25: 3.
37 Green, M.A., Hishikawa, Y., Warta, W. et al. (2017). *Prog. Photovoltaics Res. Appl.* 25: 668.
38 Green, M.A., Hishikawa, Y., Dunlop, E.D. et al. (2018). *Prog. Photovoltaics Res. Appl.* 26: 3.
39 Green, M.A., Hishikawa, Y., Dunlop, E.D. et al. (2018). *Prog. Photovoltaics Res. Appl.* 26: 427.
40 Green, M.A., Hishikawa, Y., Dunlop, E.D. et al. (2019). *Prog. Photovoltaics Res. Appl.* 27: 3.

41 Green, M.A., Dunlop, E.D., Levi, D.H. et al. (2019). *Prog. Photovoltaics Res. Appl.* 27: 565.

42 Green, M.A., Dunlop, E.D., Hohl-Ebinger, J. et al. (2019). *Prog. Photovoltaics Res. Appl.* 28: 3.

43 Case, C., Beaumont, N., and Kirk, D. (2019). *ACS Energy Lett.* 4: 2760.

44 Bakulin, A.A., Selig, O., Bakker, H.J. et al. (2015). *J. Phys. Chem. Lett.* 6: 3663.

45 Egger, D.A., Rappe, A.M., and Kronik, L. (2016). *Acc. Chem. Res.* 49: 573.

46 Eames, C., Frost, J.M., Barnes, P.R.F. et al. (2015). *Nat. Commun.* 6: 7497.

47 Shirayama, M., Kadowaki, H., Miyadera, T. et al. (2016). *Phys. Rev. Appl.* 5: 014012.

48 Fujiwara, H. and Collins, R.W. (2018). *Spectroscopic Ellipsometry for Photovoltaics: Volume 2: Applications and Optical Data of Solar Cell Materials*. Cham, Switzerland: Springer.

49 Yamada, Y., Nakamura, T., Endo, M. et al. (2014). *Appl. Phys. Express* 7: 032302.

50 Ndione, P.F., Li, Z., and Zhu, K. (2016). *J. Mater. Chem. C* 4: 7775.

51 Zhao, B., Abdi-jalebi, M., Tabachnyk, M. et al. (2017). *Adv. Mater.* 29: 1604744.

52 de Quilettes, D.W., Koch, S., Burke, S. et al. (2016). *ACS Energy Lett.* 1: 438.

53 Metzger, W.K., Repins, I.L., and Contreras, M.A. (2008). *Appl. Phys. Lett.* 93: 022110.

54 Phuong, L.Q., Okano, M., Yamada, Y. et al. (2014). *Appl. Phys. Lett.* 104: 081907.

55 Stranks, S.D., Eperon, G.E., Grancini, G. et al. (2013). *Science* 342: 341.

56 Xing, G., Mathews, N., Sun, S. et al. (2013). *Science* 342: 344.

57 Stolterfoht, M., Wolff, C.M., Márquez, J.A. et al. (2018). *Nat. Energy* 3: 847.

58 Tan, H., Jain, A., Voznyy, O. et al. (2017). *Science* 355: 722.

59 Nakane, A., Tampo, H., Tamakoshi, M. et al. (2016). *J. Appl. Phys.* 120: 064505.

60 Stoumpos, C.C., Malliakas, C.D., and Kanatzidis, M.G. (2013). *Inorg. Chem.* 52: 9019.

61 Dang, Y., Liu, Y., Sun, Y. et al. (2015). *CrystEngComm* 17: 665.

62 Breternitz, J., Lehmann, F., Barnett, S.A. et al. (2020). *Angew. Chem. Int. Ed.* 59: 424.

63 Poglitsch, A. and Weber, D. (1987). *J. Chem. Phys.* 87: 6373.

64 Chen, T., Foley, B.J., Ipek, B. et al. (2015). *Phys. Chem. Chem. Phys.* 17: 31278.

65 Stolterfoht, M., Caprioglio, P., Wolff, C.M. et al. (2019). *Energy Environ. Sci.* 12: 2778.

66 Giorgi, G., Fujisawa, J.-I., Segawa, H., and Yamashita, K. (2013). *J. Phys. Chem. Lett.* 4: 4213.

67 Mosconi, E., Amat, A., Nazeeruddin, M.K. et al. (2013). *J. Phys. Chem. C* 117: 13902.

68 Baikie, T., Fang, Y., Kadro, J.M. et al. (2013). *J. Mater. Chem. A* 1: 5628.

69 Yin, W.-J., Yang, J.-H., Kang, J. et al. (2015). *J. Mater. Chem. A* 3: 8926.

70 Fujiwara, H., Kato, M., Tamakoshi, M. et al. (2018). *Phys. Status Solidi A* 215: 1700730.

71 Yamada, Y., Nakamura, T., Endo, M. et al. (2014). *J. Am. Chem. Soc.* 136: 11610.

72 Yang, Y., Yang, M., Li, Z. et al. (2015). *J. Phys. Chem. Lett.* 6: 4688.

73 Manser, J.S. and Kamat, P.V. (2014). *Nat. Photon.* 8: 737.

74 Yang, Y., Ostrowski, D.P., France, R.M. et al. (2016). *Nat. Photon.* 10: 53.
75 Savenije, T.J., Ponseca, C.S. Jr., Kunneman, L. et al. (2014). *J. Phys. Chem. Lett.* 5: 2189.
76 Wehrenfennig, C., Eperon, G.E., Johnston, M.B. et al. (2014). *Adv. Mater.* 26: 1584.
77 Milot, R.L., Eperon, G.E., Snaith, H.J. et al. (2015). *Adv. Funct. Mater.* 25: 6218.
78 De Wolf, S., Holovsky, J., Moon, S.-J. et al. (2014). *J. Phys. Chem. Lett.* 5: 1035.
79 Nishiwaki, M., Nagaya, K., Kato, M. et al. (2018). *Phys. Rev. Mater.* 2: 085404.
80 Lin, Q., Armin, A., Nagiri, R.C.R. et al. (2015). *Nat. Photonics* 9: 106.
81 Miyata, A., Mitioglu, A., Plochocka, P. et al. (2015). *Nat. Phys.* 11: 582.
82 Sendner, M., Nayak, P.K., Egger, D.A. et al. (2016). *Mater. Horiz.* 3: 613.
83 Dong, Q., Fang, Y., Shao, Y. et al. (2015). *Science* 347: 967.
84 Semonin, O.E., Elbaz, G.A., Straus, D.B. et al. (2016). *J. Phys. Chem. Lett.* 7: 3510.
85 Bi, Y., Hutter, E.M., Fang, Y. et al. (2016). *J. Phys. Chem. Lett.* 7: 923.
86 Shi, D., Adinolfi, V., Comin, R. et al. (2015). *Science* 347: 519.
87 Hutter, E.M., Eperon, G.E., Stranks, S.D., and Savenije, T.J. (2015). *J. Phys. Chem. Lett.* 6: 3082.
88 Chen, Y., Yi, H.T., Wu, X. et al. (2016). *Nat. Commun.* 7: 12253.
89 Saidaminov, M.I., Abdelhady, A.L., Murali, B. et al. (2015). *Nat. Commun.* 6: 7586.
90 Yang, T.-Y., Gregori, G., Pellet, N. et al. (2015). *Angew. Chem.* 127: 8016.
91 Futscher, M.H., Lee, J.M., McGovern, L. et al. (2019). *Mater. Horiz.* 6: 1497.
92 Bertoluzzi, L., Boyd, C.C., Rolston, N. et al. (2020). *Joule* 4: 109.
93 Herz, L.M. (2018). *J. Phys. Chem. Lett.* 9: 6853.
94 Frost, J.M. (2017). *Phys. Rev. B* 96: 195202.
95 Rakita, Y., Cohen, S.R., Kedem, N.K. et al. (2015). *MRS Commun.* 5: 623.
96 Feng, J. (2014). *APL Mater.* 2: 081801.
97 Kawamura, Y., Mashiyama, H., and Hasebe, K. (2002). *J. Phys. Soc. Jpn.* 71: 1694.
98 Onoda-Yamamuro, N., Matsuo, T., and Suga, H. (1990). *J. Phys. Chem. Solids* 51: 1383.
99 Pisoni, A., Jaćimović, J., Barišić, O.S. et al. (2014). *J. Phys. Chem. Lett.* 5: 2488.
100 Weller, M.T., Weber, O.J., Henry, P.F. et al. (2015). *Chem. Commun.* 51: 4180.
101 Xing, G., Mathews, N., Lim, S.S. et al. (2014). *Nat. Mater.* 13: 476.
102 Braly, I.L., de Quilettes, D.W., Pazos-Outón, L.M. et al. (2018). *Nat. Photonics* 12: 355.
103 Wang, Q., Shao, Y., Xie, H. et al. (2014). *Appl. Phys. Lett.* 105: 163508.
104 Hou, Y., Aydin, E., De Bastiani, M. et al. (2020). *Science* 367: 1135.
105 Jošt, M., Kegelmann, L., Korte, L., and Albrecht, S. (2020). *Adv. Energy Mater.* 10: 1904102.
106 Hoke, E.T., Slotcavage, D.J., Dohner, E.R. et al. (2015). *Chem. Sci.* 6: 613.
107 Brennan, M.C., Draguta, S., Kamat, P.V., and Kuno, M. (2018). *ACS Energy Lett.* 3: 204.
108 Jošt, M., Lipovšek, B., Glažar, B. et al. (2020). *Adv. Energy Mater.* 10: 2000454.

109 From product data sheet of "Cheetah HC 72M 390–410 Watt" (Jinko Solar).
110 From product data sheet of "KuMax CS3U-375/380MS" (CanadianSolar).
111 From product data sheet of "ASM-7-PERC-375" (Adani Solar).
112 Mishima, T., Taguchi, M., Sakata, H., and Maruyama, E. (2011). *Sol. Energy Mater. Sol. Cells* 95: 18.
113 From product data sheet of "SF175-S" (Solar Frontier).
114 From product data sheet of "SF170-S" (Solar Frontier).
115 Niu, G., Guo, X., and Wang, L. (2015). *J. Mater. Chem. A* 3: 8970.
116 Berhe, T.A., Su, W.-N., Chen, C.-H. et al. (2016). *Energy Environ. Sci.* 9: 323.
117 Leijtens, T., Eperon, G.E., Noel, N.K. et al. (2015). *Adv. Energy Mater.* 5: 1500963.
118 Wang, D., Wright, M., Elumalai, N.K., and Uddin, A. (2016). *Sol. Energy Mater. Sol. Cells* 147: 255.
119 Wang, R., Mujahid, M., Duan, Y. et al. (2019). *Adv. Funct. Mater.* 29: 1808843.
120 Kim, H.-S., Seo, J.-Y., and Park, N.-G. (2016). *ChemSusChem* 9: 2528.
121 Shirayama, M., Kato, M., Miyadera, T. et al. (2016). *J. Appl. Phys.* 119: 115501.
122 Eperon, G.E., Stranks, S.D., Menelaou, C. et al. (2014). *Energy Environ. Sci.* 7: 982.
123 Lee, J.-W., Kim, D.-H., Kim, H.-S. et al. (2015). *Adv. Energy Mater.* 5: 1501310.
124 Li, Z., Yang, M., Park, J.-S. et al. (2016). *Chem. Mater.* 28: 284.
125 Yi, C., Luo, J., Meloni, S. et al. (2016). *Energy Environ. Sci.* 9: 656.
126 McMeekin, D.P., Sadoughi, G., Rehman, W. et al. (2016). *Science* 351: 151.
127 Chen, P., Bai, Y., Wang, S. et al. (2018). *Adv. Funct. Mater.* 28: 1706923.
128 Cho, K.T., Grancini, G., Lee, Y. et al. (2018). *Energy Environ. Sci.* 11: 952.
129 Jung, E.H., Jeon, N.J., Park, E.Y. et al. (2019). *Nature* 567: 511.
130 Chaudhary, B., Kulkarni, A., Jena, A.K. et al. (2017). *ChemSusChem* 10: 2473.
131 Wang, F., Shimazaki, A., Yang, F. et al. (2017). *J. Phys. Chem. C* 121: 1562.
132 Gu, S., Lin, R., Han, Q. et al. (2020). *Adv. Mater.* 32: 1907392.
133 New Energy and Industrial Technology Development Organization (NEDO) and Panasonic Corporation (2020). Photograph of the large-area module is taken from https://www.nedo.go.jp/english/news/AA5en_100421.html with permission.
134 Li, Z., Klein, T.R., Kim, D.H. et al. (2018). *Nat. Rev. Mater.* 3: 18017.
135 Fuiwara, H. and Collins, R.W. (2018). *Spectroscopic Ellipsometry for Photovoltaics: Volume 1: Fundamental Principles and Solar Cell Characterization*. Cham, Switzerland: Springer.
136 Koida, T. (2017). *Phys. Status Solidi A* 214: 1600464.
137 Babayigit, A., Thanh, D.D., Ethirajan, A. et al. (2016). *Sci. Rep.* 6: 18721.
138 Babayigit, A., Ethirajan, A., Muller, M., and Conings, B. (2016). *Nat. Mater.* 15: 247.
139 Ju, M.-G., Chen, M., Zhou, Y. et al. (2018). *Joule* 2: 1231.